

Supplementary Information

Reconfigurable Artificial Synapses Using an Organic Antiambipolar Transistor for Brain-inspired Computing

Ryoma Hayakawa, ^{*,a} Yuho Yamamoto, ^{a,b} Kosuke Yoshikawa, ^{a,b} Yoichi Yamada^b and Yutaka Wakayama^{*,a}

^aResearch Center for Materials Nanoarchitectonics (MANA), National Institute for Materials Science (NIMS), 1-1 Namiki, Tsukuba 305-0044, Japan

^bFaculty of Pure and Applied Sciences, University of Tsukuba 1-1-1 Tennodai, Tsukuba 305-8573, Japan

1. Optimization of growth conditions of the constituent layers of FG-OAAT

First, we optimized the surface morphology of Au FG electrode because the surface morphology closely affects the surface roughness of the HfO₂ tunneling layer and the organic channel layers. Figure S1 shows the atomic force microscope (AFM) images of Au FG electrodes with different deposition rates. The surface roughness of Au layer reduced by increasing the deposition rate and consequently reached 0.30 nm at the deposition rate of 5 Å/s.

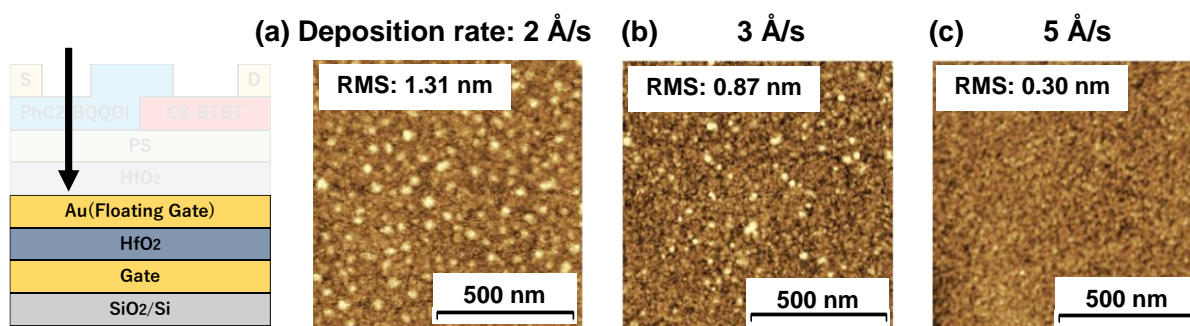


Figure S1 AFM images of Au thin films with different deposition rates: (a) 2 Å/s, (b) 3 Å/s and (c) 5 Å/s.

Figure S2 shows the AFM images of HfO₂ (tunneling layer) and organic channel layers formed on the optimized Au FG electrode. The film thicknesses of PhC₂-BQQDI and C8-BTBT

were measured by the line profile of AFM images as shown in Figure S3. The estimated film thicknesses were 8 ± 2 nm for PhC₂-BQQDI and 13 ± 3 nm for C8-BTBT, respectively.

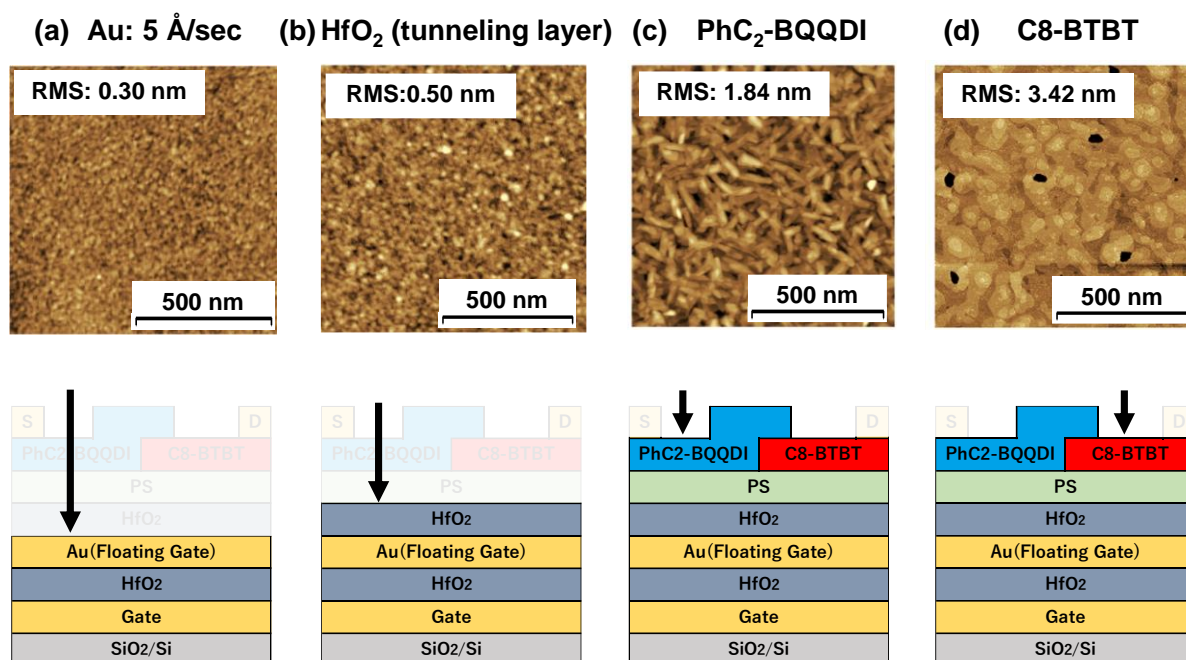


Figure S2 AFM images of (a) the optimized Au FG electrode, (b) HfO₂ tunneling layer, (c) PhC₂-BQQDI and (d) C8-BTBT layers. It is noted that (a) is duplication of S1(c).

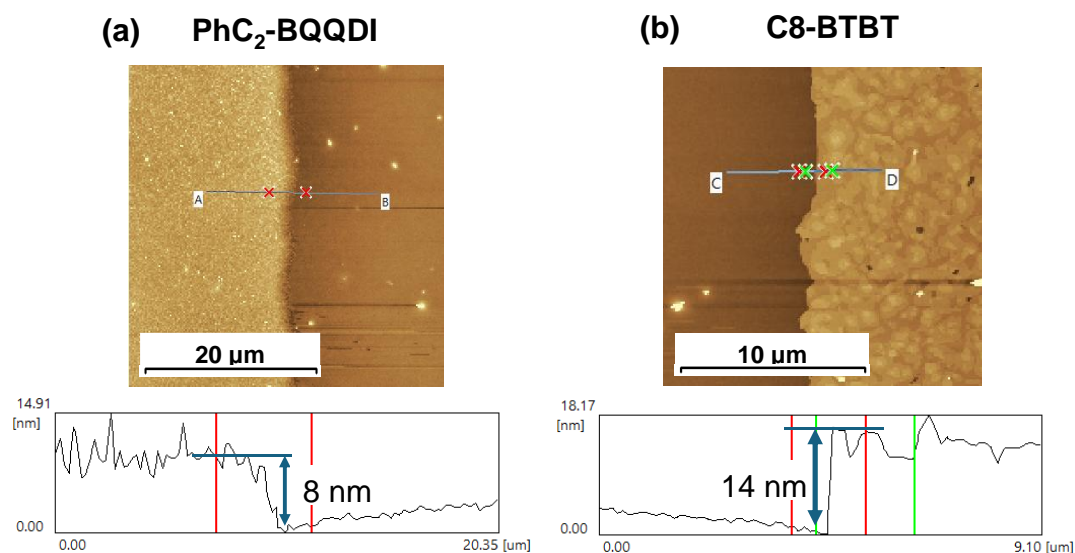


Figure S3 AFM images and line profiles of (a) PhC₂-BQQDI and (b) C8- BTBT layers.

2. Optimization of thickness of HfO₂ bottom-gate insulating layer

Figure S4 exhibits the drain current (I_D) and bottom-gate current (I_{BG}) of FG-OAATs as a function of bottom-gate (BG) voltages (V_{BG}), where 30 and 35 nm-thick HfO₂ layer were employed as BG insulating layers.

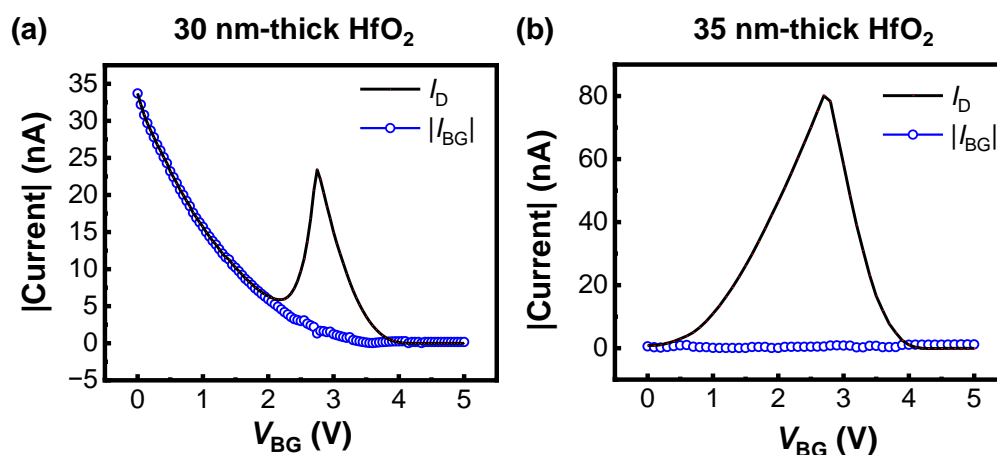


Figure S4 I_D and I_G plots of FG-OAATs as function of V_{BG} , where (a) 30 nm- and (b) 35 nm-thick HfO₂ BG insulating layers were used, respectively.

In the sample with 30 nm-thick HfO₂ BG insulating layer, I_D and $|I_{BG}|$ were identical, indicating that I_{BG} flew from the BG to drain electrodes through the FG electrode (Figure S4 (a)). Meanwhile, I_{BG} was completely suppressed in the sample with 35 nm-thick HfO₂ BG insulating layer (Figure S4 (b)). Therefore, we used the 35 nm-thick HfO₂ BG insulating layer in this manuscript.

3. Optimization of film thickness of organic channel layers

We evaluated I_D - V_{BG} curves of PhC₂-BQQDI and C8-BTBT transistors with different film thicknesses. Figures S5 (a) and (b) show the estimated electron mobilities and threshold voltages of PhC₂-BQQDI transistors, respectively. Figures S5 (c) and (d) indicate the estimated hole mobilities and threshold voltages of C8-BTBT transistors, respectively.

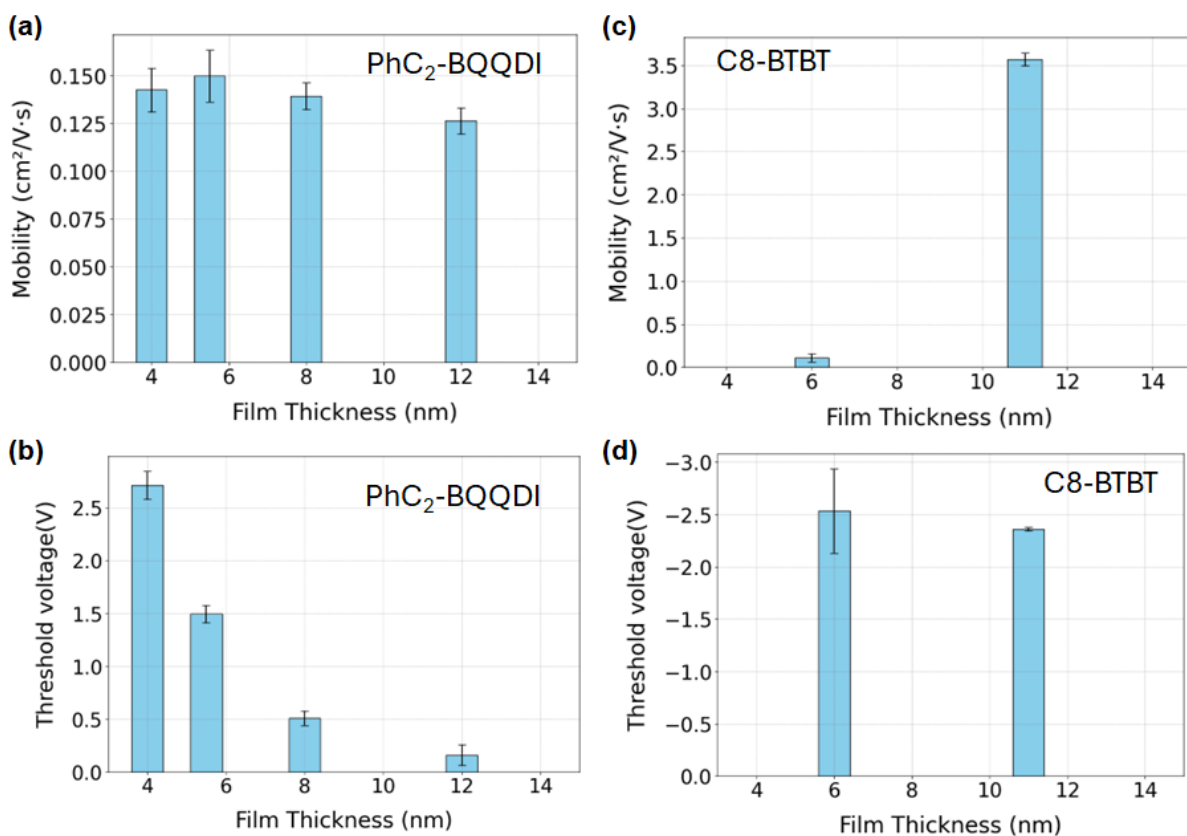


Figure S5 (a) Electron mobilities and (b) threshold voltages of PhC₂-BQQDI transistors. (c) Hole mobilities and (b) threshold voltages of C8-BTBT transistors.

The electron mobility was calculated to be 0.14 cm²/Vs in 4 nm-thick PhC₂-BQQDI transistors. The value was almost identical in samples with the film thickness of up to 8 nm (Figure S5 (a)). However, the electron mobility decreased in the samples with film thickness of above 8 nm, although the threshold voltage still slightly reduced. Based on the above analysis, 8 nm-thick PhC₂-BQQDI layer was used as the n-type transistor channel to satisfy both factors of high electron mobility and low threshold voltage.

For C8-BTBT transistors, hole mobilities of around 3 cm²/Vs were obtained in the samples with film thickness of above 10 nm (Figure S5 (c)). However, the hole mobility markedly decreased in samples with the film thickness of below 11 nm, although the threshold voltages were almost constant (Figure S5 (d)). Throughout the above measurements, 13 nm-thick C8-BTBT layer was employed as the p-type transistor channel in this manuscript.

4. Analysis of LTP/LTD curves

Figure S6 represents the conductance curves as a function of pulse numbers. The conductance values were calculated from Figures 3(b)-(d) in the manuscript. It is noted that the conductance was normalized by the maximum value. The nonlinearity coefficient (α) and asymmetry factor (ν) were calculated using the following equations:^{S1,S2}

$$G_p = G_1(1 - e^{-\alpha_p N}) + G_{min} \quad (1)$$

$$G_D = G_{max} - G_1[1 - e^{-\alpha_d(N_{max}-N)}] \quad (2)$$

$$G_1 = \frac{(G_{max}-G_{min})}{(1-e^{-\alpha N_{max}})} \quad (3)$$

$$\nu = \alpha_p - \alpha_d \quad (4)$$

Here, G_p and G_D are the conductance values for respective potentiation and depression properties. G_{max} and G_{min} are the maximum and minimum conductance values, respectively. N and N_{max} are the pulse number and maximum pulse number, respectively. G_1 is the function of α to fit the G_p and G_D curves within the range of G_{max} , G_{min} , and N_{max} .

The nonlinearity coefficients for potentiation (α_p) and depression (α_d) are calculated by fitting the equations (1)-(3). When $\nu = 0$, the conductance update is ideally linear. The asymmetry factor is defined by the difference of nonlinearity factors in the potentiation and depression and given as equation (4).^{S2} Importantly, the application of continuous presynaptic pulses improved the nonlinearity coefficients and asymmetry factors. The nonlinearity coefficients of $\alpha_p = 1.1$ and $\alpha_d = -0.9$ are smaller than those of conventional ones,^{S1,S3,S4} which is a benefit to use the FG-OAAT for neuromorphic applications.

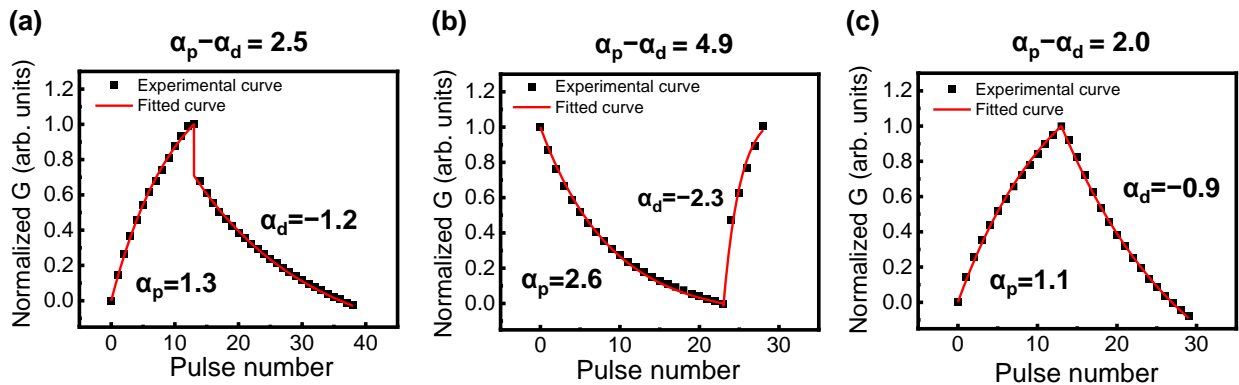


Figure S6(a) LTP and LTD operations as a function of presynaptic pulse numbers, where the

polarity of input pulse voltage was reversed. (b) LTD and LTP as a function of presynaptic pulse numbers, where the polarity of input pulse voltage was reversed. (c) Transition from LTP to LTD induced by continuous presynaptic pulses.

5. Analysis of PPF/PPD curves

Figure S7 shows PPF and PPD curves as a function of pulse numbers. It is noted that the figures are duplications of Figures 4 (c) and (f) in the manuscript. The curves can be generally fitted using the following equations:^{S5,S6}

$$\text{PPF or PPD index} = A_1 e^{\left(\frac{-\Delta t}{\tau_1}\right)} + A_2 e^{\left(\frac{-\Delta t}{\tau_2}\right)} \quad (5)$$

where Δt is the pulse interval time, A_1 and A_2 are the initial amplitudes, and τ_1 and τ_2 represent the relaxation times of two phases, respectively. The PPF and PPD curves were well fitted by equation (5). The τ_1 and τ_2 were extracted as 3 s and 162 s for the PPF curve (Figure S7 (a)). Meanwhile, the τ_1 and τ_2 were calculated to be 2 s and 120 s for the PPD curve (Figure S7(b)).

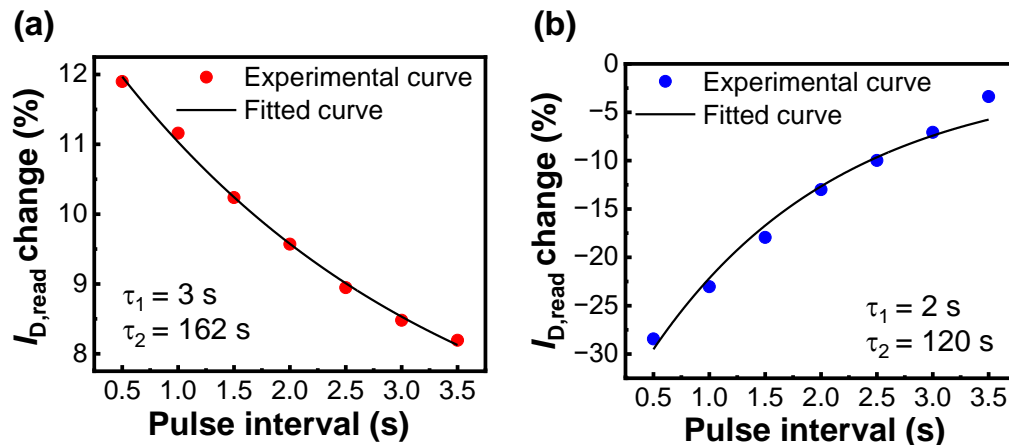


Figure S7 (a) PPF and PPD operations of the FG-OAAT. It is noted that (a) and (b) are duplications of Figures 4 (c) and (f) in the manuscript.

References

- S1. J. Kang, T. Kim, S. Hu, J. Kim, J. Y. Kwak, J. Park, J. K. Park, I. Kim, S. Lee, S. Kim and Y. Jeong, *Nat. Commun.*, 2022, **13**, 4040.
- S2. S. Park, S. Seong, G. Jeon, W. Ji, K. Noh, S. Kim, and Y. Chung, *Adv. Electron. Mater.*,

2023, **9**, 2200554.

S3. S. Seo, B.-S. Kang, J.-J. Lee, H.-J. Ryu, S. Kim, H. Kim, S. Oh, J. Shim, K. Heo, S. Oh and J.-H. Park, *Nat. Commun.*, 2020, **11**, 3936.

S4. D. P. Sahu, K. Park, P. H. Chung, J. Han and T.-S. Yoon, *Sci. Rep.* 2023, **13**, 9592.

S5. Y. Bu, T. Xu, S. Geng, S. Fan, Q. Li and J. Su, *Adv. Funct. Mater.*, 2023, **33**, 2213741.

S6. C. Han, X. Han, J. Han, M. He, S. Peng, C. Zhang, X. Liu, J. Gou and J. Wang, *Adv. Funct. Mater.*, 2022, **32**, 2113053.